Full Paper

Journal of the Brazilian Chemical Society

https://dx.doi.org/10.21577/0103-5053.20250127

J. Braz. Chem. Soc. **2025**, *36*, 12, e-20250127, 1-11

Cobalt-Nickel Nanocatalyst Supported on Phosphorus-Doped Hydrochar from Malt Bagasse Waste Synthesized via One-Pot Wet Pyrolysis for Safe and Sustainable Hydrogen Fuel Evolution from Sodium Borohydride

Marcela M. Ferreira,[a] ***Gessica C. Dias,***[a] ***Tatianny A. Andradre,***[a] ***Iterlandes Machado Junior,***[a]
José O. Marques Neto,[a] ***Aline Aparecida S. Silva,***[a] ***Renata P. L. Moreira***[a] ***and Tiago A. Silva****[,a]

[a]*Departamento de Química, Universidade Federal de Viçosa, Av. Peter Henry Rolfs, s/n,*
Campus Universitário, 36570-900 Viçosa-MG, Brazil

Hydrogen (H_2) fuel has emerged as a clean and sustainable energy source, however, efficient and safe storage of H_2 remains challenging. This study synthesized phosphorus-doped hydrochar (HC) from malt bagasse waste (BSG) using hydrothermal process with phosphoric acid (H_3PO_4) activation in a one-pot reaction, known as wet pyrolysis, under mild synthesis conditions. The HC was then used as a carbon support for cobalt (Co) and nickel (Ni) nanoparticles to catalyze H_2 evolution from the solid-state chemical store sodium borohydride ($NaBH_4$). The nanocatalysts were characterized using various techniques, including transmission electron microscopy (TEM), Fourier transform infrared spectroscopy (FTIR), X-ray diffraction (XRD) and Brunauer-Emmett-Teller (BET) analysis. In the H_2 evolution reaction from $NaBH_4$, the catalysts demonstrated notable catalytic efficiency, with hydrogen generation rates of 2193.17 mL min^{-1} g^{-1} for monometallic (Co NPs-HC) and 1205.74 mL min^{-1} g^{-1} for bimetallic composition (Co/Ni NPs-HC (80:20)). Additionally, the bimetallic Co-Ni nanocatalyst exhibited stronger stability, maintaining performance over up to six reuse cycles. These findings highlight the potential of the developed nanocatalysts for practical applications in safe hydrogen generation processes, in addition to promoting the circular economy through the reuse and aggregation of value to BSG generated in tons annually by the beer industry.

Keywords: biomass waste, one-pot hydrothermal synthesis, biochar, catalysis, hydrogen fuel, sodium borohydride

Introduction

The global beer industry produces approximately 90 tons of malt bagasse waste (BSG) annually. For every 100 L of beer produced, 45 kg of BSG are generated, making it the most abundant by-product of beer production.[1] BSG is commonly used as animal feed, for biogas production, or disposed of in landfills.[2] Finding ways to exploit the full potential of BSG not only adds value to the by-product but fosters a circular economy.

One approach involves converting BSG into hydrochar (HC), a versatile material with potential applications in contaminant adsorption,[3] energy storage,[4] soil amendment[5] and catalysis.[6] This conversion can be achieved through hydrothermal carbonization (HTC), a process that occurs under subcritical water conditions, with temperatures between 100 and 374 °C and pressures above atmospheric. In this range, water remains liquid but with properties intermediate between the liquid and supercritical states, making it effective as a solvent or reactive medium in biomass decomposition reactions, such as the conversion of waste into hydrochar.[7] This material is different from pyrochar, which is obtained from dry pyrolysis that occurs at high temperatures in an inert atmosphere. In addition to the milder synthesis conditions, a key advantage of HTC is that the biomass does not require pre-drying before the process, as the water content can be effectively utilized in the hydrothermal conversion.

The HC applications are made possible by their inherent properties, such as high surface area and porosity, which can be further enhanced through chemical or physical activation.[7] Baytar *et al*.[8] synthesized hydrochars from pinecones and *Rheum ribes* peels and used them in the hydrolysis of sodium borohydride under microwave irradiation at different temperatures. It is important to highlight those different types of biomasses produce biochars with distinct properties, making the investigation

---

*e-mail: tiago.a.silva@ufv.br

Editor handled this article: Izaura C. N. Diógenes (Executive)

of their characteristics and potential applications essential.

The hydrothermal carbonization of BSG by one-pot activation with phosphoric acid (H_3PO_4) results in a material with a significantly increased surface area, attributed to the introduction of various oxygen-containing functional groups on its surface.[1] Phosphorus (P) doping improves the adsorption performance of the material. P's lower electronegativity and larger covalent radius, compared to other heteroatoms like nitrogen and sulfur, enhance this effect.[9] An important and unexplored application of BSG hydrochar is its use as a catalyst support in the generation of hydrogen (H_2) fuel through the hydrolysis of sodium borohydride ($NaBH_4$). For this purpose, the support must possess a high surface area and effectively prevent particle agglomeration from preserving the specific surface area.[10]

Currently, one of the most significant challenges facing humanity is climate change caused by the emission of greenhouse gases (GHGs), part of which originates from the production of electricity,[11] in addition to the depletion of fossil fuel sources. Considering this scenario, there is an urgent need for sustainable energy alternatives.[12] Hydrogen gas emerges as a promising clean and renewable energy source,[13] with water as the only byproduct of its combustion and a calorific value of 142 MJ kg^{-1}, higher than fossil fuels such as gasoline, methanol, and diesel.[14] The H_2 can be stored in gaseous, liquid, and solid states. In its gaseous form, H_2 is compressed and stored in carbon fiber tanks, a method that is both costly and raises significant safety concerns due to the high volumetric density and extreme pressure required, which increases the risk of explosions. Additionally, storing H_2 as a liquid involves high energy consumption during liquefaction and the potential for evaporation losses.[15]

Solid-state H_2 storage is both safe and efficient, with applications across a range of materials, including metal alloys,[16] zeolites,[17] two-dimensional metal-organic frameworks (MOFs),[18] and metal hydrides,[19] among others. According to the United States Department of Energy (DOE),[20] an ideal material for solid H_2 storage should have a gravimetric density exceeding 6.5% by weight and a H_2 binding energy between 0.2 and 0.7 eV *per* H_2. Additionally, evaluating application conditions, such as reaction temperature, is crucial. The $NaBH_4$ is a stable solid H_2 storage medium and its solution are non-flammable. The hydrolysis of $NaBH_4$ produces a safe byproduct and enables the storage of 10.8% by weight of hydrogen.[10] The hydrolysis reaction is described by equation 1.

$$NaBH_{4(aq)} + 2H_2O_{(l)} \rightarrow NaBO_{2(aq)} + 4H_{2(g)} \quad 216.18\ \text{kJ} \quad (1)$$

The reaction exhibits slow kinetics, which makes using metallic nanocatalysts supported on carbon-based materials a common approach. Noble metals, such as platinum (Pt),[21] palladium (Pd)[22] and ruthenium (Ru),[23] are frequently used as catalyst nanoparticles for hydrogen generation from $NaBH_4$. However, due to their high cost and limited availability, there is growing interest in exploring lower-cost alternatives using non-noble metals. Metals such as nickel (Ni),[24] cobalt (Co),[25] iron (Fe)[26] and copper (Cu)[27] are increasingly being investigated. These non-noble metals are often employed in bimetallic catalysts to enhance performance and reduce costs.[28]

Among the non-noble metals used as catalysts for $NaBH_4$ hydrolysis, Co is economically attractive due to its widespread availability and low cost. Moreover, it exhibits high catalytic activity, excellent stability, and versatile coordination chemistry.[29,30] These traits facilitate its incorporation into various matrices, including metallic supports, oxides, carbon-based materials, and porous structures.[31,32]

In this context, the study aimed to synthesize a phosphorus-doped hydrochar from BSG using a hydrothermal process by one-pot activation with phosphoric acid (H_3PO_4), which was then explored as a support for Co and Ni nanoparticles in H_2 evolution from $NaBH_4$. P-doping of hydrochar for the application explored in this work is interesting because it can introduce active sites and improve electronic conductivity by changes in the electronic structure and charge delocalization.[33,34] Initially, the hydrochar was characterized using various analytical techniques. Subsequently, it was employed in H_2 evolution experiments, where the effects of several variables on the process were assessed: (*i*) different metals (Co, Ni, and Pd), (*ii*) bimetallic compositions of Ni and Co, (*iii*) sodium hydroxide (NaOH) concentration, (*iv*) reaction temperature, (*v*) material reuse, and (*vi*) durability. From these experiments, the hydrogen generation rate and activation energy were evaluated.

Experimental

Reagents

Analytical-grade reagents were utilized in this study. Sodium borohydride (98%, CAS 16940-66-2) and sodium hydroxide microbeads (97%, CAS 1310-73-2) were obtained from Neon. Nickel sulfate heptahydrate (98%, CAS 10101-98-1), cobalt nitrate hexahydrate (98%, CAS 10026-22-9), potassium tetrachloropalladate(II) (98%, CAS 10025-98-6) and deuterated water (D_2O, 99.8%, CAS 7789-20-0) were purchased from Sigma-Aldrich. Malt bagasse was supplied by the Laboratory of Fermented and Distilled Beverages, located in the Department of Chemistry of the Federal University of Viçosa. All solutions were prepared using type 1 ultrapure water (resisitvity > 18.2 MΩ cm) provided by the Milli-Q system.

Hydrochar synthesis

The BSG was dried in an oven at 105 °C for 24 h, then ground using a blender, sieved through a 35-mesh sieve (0.5 mm opening), and stored at room temperature. The processed BSG was subsequently subjected to a one-pot hydrothermal carbonization process. Precisely, 5 g of the material were placed in a 100 mL Teflon-lined stainless-steel autoclave. A 50.0 mL volume of a 0.1 mol L^{-1} phosphoric acid solution was added as an activating agent.[35] The system was then heated in an oven at 150 °C for 14 h, after which it was allowed to cool to room temperature.

The obtained material was washed with deionized water until it reached pH 7.0. The sample was centrifuged for 20 min at 4000 rpm between each washing step, according to the method adapted from de Oliveira Fontoura *et al*.[3] After carbonization, the sample was dried in an oven at 105 °C for 24 h. The resulting hydrochar was then stored at room temperature.

Synthesis of hydrochar-supported nanoparticles

To synthesize hydrochar-supported nanoparticles, 10 mg of hydrochar was dispersed in 3 mL of water. Next, an appropriate amount of the desired metal precursor salt, $Co(NO_3)_2•6H_2O$, $NiSO_4•7H_2O$, or K_2PdCl_4, as detailed in Table 1, was dissolved in 2 mL of ultrapure water, maintaining a total catalyst amount of 0.04 mmol. The mixture was stirred at room temperature (ca. 25 °C) for 15 min. Subsequently, 2.00 mL of a $NaBH_4$ solution (0.25 mol L^{-1}) was added, and the system was stirred for an additional 15 min. The material then underwent a washing step followed by centrifugation (4000 rpm for 7 min), with this process repeated three times. Six different compositions of hydrochar-supported nanoparticles were prepared, as outlined in Table 1.

Material characterization

X-ray diffraction (XRD) analysis was performed using a Bruker diffraction system, model D8-Discover, with Cu Kα radiation (λ = 0.1541 nm) and a 2θ angular range from 10° to 50°. Morphological analysis was conducted using transmission electron microscopy (TEM). TEM analyses were performed using specific equipment, the Tecnai G2-20 - SuperTwin FEI-200 kV, equipped with an energy dispersive X-ray spectrometer (EDS). EDS analysis was performed using a silicon drift detector with a resolution of 133 eV. Functional groups in the material were analyzed using Fourier transform infrared spectroscopy (FTIR) with a VARIAN 660-IR instrument, equipped with a PIKE GladiATR accessory featuring a diamond crystal. Transmittance was measured over the wavenumber range of 4000 to 600 cm^{-1}. Nitrogen adsorption and desorption isotherms were obtained using a Nova 600 Series instrument (Anton Paar). Before measurements, the samples were vacuum-dried at 120 °C for 4 h to remove any residual water and gases. The surface area was calculated using the Brunauer-Emmett-Teller (BET) method, and the pore size distribution was determined by the Barrett-Joyner-Halenda (BJH) method.

Table 1. Composition of nanoparticles (NPs) supported on hydrochar (HC)

NPs / %	Code	n NPs ratio / mmol
Co (100)	Co NPs-HC[a]	100/0
Co/Ni (80:20)	Co/Ni NPs-HC (80:20)[b]	80/20
Co/Ni (60:40)	Co/Ni NPs-HC (60:40)	60/40
Co/Ni (50:50)	Co/Ni NPs-HC (50:50)	50/50
Co/Ni (40:60)	Co/Ni NPs-HC (40:60)	40/60
Co/Ni (20:80)	Co/Ni NPs-HC (20:80)	20/80
Ni (100)	Ni NPs-HC[c]	0/100
Pd (100)	Pd NPs-HC[d]	0/100

[a]Co NPs-HC: pure cobalt nanoparticles supported on P-doped hydrochar; [b]Co/Ni NPs-HC (80:20): bimetallic cobalt and nickel nanoparticles consisting of 80% Co and 20% Ni by mole supported on P-doped hydrochar. The same applies to the other bimetallic nanoparticles, only changing the molar ratio between Co and Ni; [c]NiNPs-HC: pure nickel nanoparticles supported on P-doped hydrochar; [d]Pd NPs-HC: pure palladium nanoparticles supported on P-doped hydrochar.

The P content of the doped hydrochar sample was determined. Phosphorus extraction was performed using an adapted Melich-1 extractor for the hydrochar sample, using a solution containing 0.0125 mol L^{-1} H_2SO_4 and 0.05 mol L^{-1} HCl. The extractant solution:solid ratio was 1:10, i.e., 1 g of solid sample to 10 mL of extractant solution. 2 g of hydrochar and 20 mL of extractant were used. The system was stirred for 1 h at 120 rpm, after which the mixture was filtered through quantitative filter paper. The extract was diluted 500-fold for spectrophotometric determination of phosphorus. Phosphorus was determined by the method described by Braga and Defelipo.[36] This method uses the complexation reaction of phosphate with ammonium molybdate, forming blue ammonium phospho-molybdate, with the reading by UV-Vis spectrophotometry performed at 725 nm using a Genesys 50 spectrophotometer (Thermo Fisher Scientific) equipped with a 1 cm quartz cuvette.

Hydrogen evolution from $NaBH_4$

The freshly prepared hydrochar-supported nanoparticles were dispersed in 10.00 mL of type 1 water in a 125 mL Kitassato flask, which was sealed with a rubber septum. The system was stirred on a temperature-controlled magnetic stirrer. A rubber hose was connected to the side outlet of the Kitassato, directing the hydrogen gas to a burette. Subsequently, 1.00 mL of a $NaBH_4$ solution (0.500 mol L^{-1}) was injected into the system using a syringe, and the reaction time was monitored.

The pressure (P) generated by the H_2 gas in the liquid column was corrected using the following parameters: water density (ρ) of 1000 kg m^{-3}, gravitational acceleration (g) of 9.78 m s^{-2}, local atmospheric pressure of 94,258.65 Pa (0.93 atm), and the observed displacement (h) expressed in meters. The experiment was conducted at room temperature (25 ºC), and the absolute pressure was adjusted according to equation 2.

$$P = P_0 + \rho g h \tag{2}$$

Evaluation of reaction parameters

In the H_2 evolution tests from $NaBH_4$, the impact of four parameters was evaluated: (*i*) the composition of monometallic and bimetallic nanoparticles, (*ii*) the concentration of NaOH, (*iii*) the concentration of $NaBH_4$, (*iv*) temperature, and (*v*) the reusability and durability of the catalyst.

Evaluation of monometallic nanoparticles

The effect of monometallic nanoparticles of Co, Ni, and Pd supported on hydrochar was evaluated. The mass of the support (10 mg), the amount of metal (0.04 mmol), the volume of 1.00 mL of $NaBH_4$ (0.5 mol L^{-1}), and the temperature of 25 ºC were kept constant.

Evaluation of bimetallic nanoparticles

The effect of varying molar ratios of Co/Ni bimetallic nanoparticles (100:0, 80:20, 60:40, 50:50, 40:60, and 20:80) was evaluated (Table 1). All other conditions were kept constant, including the total catalyst amount (0.04 mmol), support mass (10 mg), $NaBH_4$ volume (1.00 mL at 0.5 mol L^{-1}), and temperature (25 ºC).

Influence of NaOH

The influence of different concentrations of NaOH (0.010; 0.050; 0.100; 0.200; 0.300; 0.400; 0.500 mol L^{-1}) was also evaluated using two nanocatalyst compositions (monometallic Co NPs-HC and bimetallic Co/Ni NPs-HC (80:20)). The total catalyst amount (0.04 mmol), support mass (10 mg), $NaBH_4$ volume (1.00 mL at 0.5 mol L^{-1}) and the temperature of 25 ºC were kept constant throughout the experiments.

Temperature

The effect of temperature (15, 25, 30 and 35 ºC) was studied using the two nanocatalyst compositions: Co NPs-HC and Co/Ni NPs-HC (80:20). In this case, the total metal content (0.04 mmol), support mass (10 mg), and $NaBH_4$ volume (1.00 mL at 0.5 mol L^{-1}) were kept constant.

Catalyst reuse and durability tests

The reusability and durability of the two nanocatalysts (Co NPs-HC and Co/Ni NPs-HC (80:20)) were evaluated under the optimal conditions identified in preliminary tests. For the reusability assessment, the mixture was centrifuged at 4000 rpm for 7 min after each reaction. The supernatant was discarded, and the catalyst was washed with type 1 water and centrifuged again. The recovered solid was then dispersed in 10.00 mL of distilled water and reintroduced into the system for the subsequent H_2 evolution reaction. This process was repeated until catalyst inactivation was observed.

The durability of the same nanocatalysts was tested under continuous stirring. At the end of each cycle, a fresh volume (1.0 mL) of $NaBH_4$ solution (0.5 mol L^{-1}) was added to the system without washing the catalyst. This procedure was repeated until catalyst inactivation occurred.

Determination of hydrogen generation rate

The hydrogen generation rate (HGR)[37] was determined according to equation 3.

$$HGR = \frac{\Delta v}{\Delta t \times m_{cat}} \tag{3}$$

where Δv is the variation in the volume of H_2 (mL), Δt is the variation in time (min), and m_{cat} is the mass of the catalyst (g).

The activation energy was calculated using the Arrhenius equation (equation 4).

$$\ln(K) = \ln(A) - \frac{E_a}{RT} \tag{4}$$

where K is the reaction kinetic constant, A is the pre-exponential factor, E_a is the apparent activation energy in kJ mol^{-1}, R is the universal gas constant, and T is the temperature in Kelvin.

Catalytic reaction mechanism

The catalytic reaction mechanism was investigated by evaluating the kinetic isotope effect (KIE) of the catalyst under previously established conditions. Specifically, 10 mg of the support (HC), 0.04 mmol of the Co/Ni NPs catalyst, and a reaction temperature of 35 °C were used. Furthermore, 1.0 mL of a freshly prepared solution containing 0.500 mol L^{-1} $NaBH_4$ in either deuterated water (D_2O) or distilled water was employed.

The KIE was determined by calculating the ratio of the rate constant for the reaction with the isotopically light reagent (k_{H_2O}) to that with the isotopically heavy reagent (k_{D_2O}), as shown in equation 5. This analysis provides valuable insights into the mechanism of the H_2 evolution reaction.

$$\text{KIE} = \frac{k_{H_2O}}{k_{D_2O}} \tag{5}$$

Results and Discussion

Material characterization

Phosphorus doped hydrochar was synthesized from malt bagasse waste using a one pot hydrothermal carbonization process and explored as a support for metallic nanoparticles to act as a catalyst in the evolution of H_2 from $NaBH_4$. The characterization of the synthesized HC is presented, as well as of the material supported with monometallic Co (Co NPs-HC) and bimetallic Co and Ni (Co/Ni NPs-HC (80:20)) nanoparticles, which demonstrated the best catalytic performance (as shown in the following sections). Figure 1 shows the XRD diffractograms of HC, Co NPs-HC, and Co/Ni NPs-HC (80:20). A notable peak is observed in the 2θ range between 15º and 30º, indicating the presence of amorphous carbon materials,[38] such as cellulose, hemicellulose, and lignina.[39] In the case of HC supporting Co and Co-Ni nanoparticles, additional peaks can be detected above 30º attributable to the incorporation of metallic nanoparticles, although of low intensity due to their lower concentration relative to the amorphous carbonaceous matrix. Particularly, the metal-phosphorus interaction of doped HC can also be mentioned from the XRD results, based on the study of Zhu *et al.*[40] who identified diffraction peaks at 31.6°, 36.3°, 46.2°, 48.1° related to cobalt phosphide (CoP) nanoparticles.

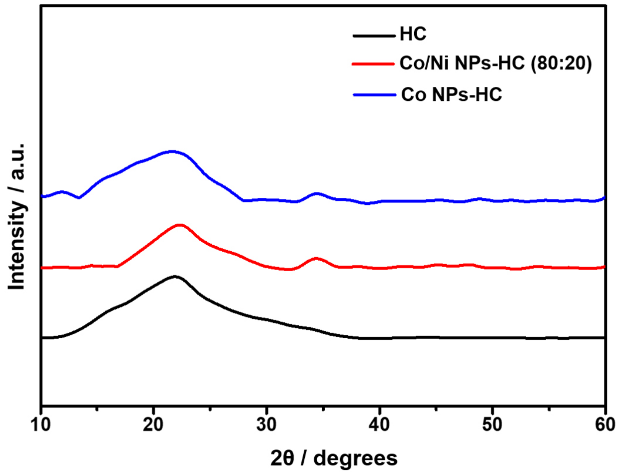

Figure 1. XRD diffractogram obtained for HC, Co NPs-HC, and Co/Ni NPs-HC (80:20).

TEM images recorded for HC support, Co NPs-HC and Co/Ni NPs-HC (80:20) are provided in Figure 2. Thus, a graphene-like morphology was verified for HC (Figure 2a), which is preserved after the deposition of nanoparticles (Figures 2b-2d). The presence of metallic nanoparticles dispersed on the HC support can be verified in both cases (Figures 2b-2d). These nanoparticles exhibited spherical shapes with an average size of approximately 60 nm, confirming the successful synthesis of the nanocatalyst. Elemental analysis by EDS was performed in selected regions, as shown in Figure S1 (see Supplementary Information (SI) section). Thus, only carbon and oxygen were detected in the graphene-like material region (area 2 of Figure S1a and EDS spectrum shown in Figure S1c), while cobalt (area 1 of Figure S1a and EDS spectrum shown in Figure S1b) and cobalt-nickel (Figure S1d and EDS spectrum shown in Figures S1e) were detected in the selected regions containing monometallic and bimetallic

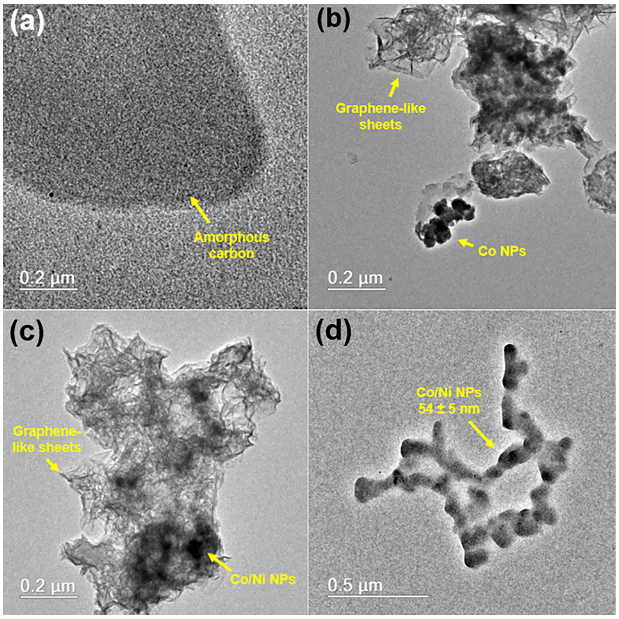

Figure 2. TEM images of (a) HC, (b) Co NPs-HC and (c, d) Co/Ni NPs-HC (80:20).

nanoparticles, evidencing the successful synthesis of the supported nanoparticles.

FTIR spectroscopy was used to analyze the functional groups of the synthesized materials. Figure 3 presents the FTIR spectrum of HC, Co NPs-HC, and Co/Ni NPs-HC (80:20). For HC, a broad band at 3388 cm^{-1} is observed, corresponding to the stretching of the O–H bond, characteristic of biochars.[3,41] The bands at 2927 and 2854 cm^{-1} are associated with the stretching vibrations of the aliphatic C–H bonds.[42] The band at 1712 cm^{-1} is attributed to the C=O stretching vibrations found in carbonyl-containing compounds such as ketones, aldehydes, and carboxylic acids, which are commonly present in biochars.[43] Additionally, the band at 1644 cm^{-1} indicates C=C stretching vibrations within aromatic rings.[44] Bands at 1063 and 1100 cm^{-1} were attributed to the C–P and P=O stretching vibrations, and the presence of bands in the 1000-750 cm^{-1} range can be associated with C–O–P and P–O–P vibrations.[9] These results reinforce the successful phosphorus doping of hydrochar. Finally, the band at 1054 cm^{-1} corresponds to the C–O stretching, characteristic of phenolic groups, alcohols, and ethers.[3,45] The functional groups in the Co NPs-HC and Co/Ni NPs-HC (80:20) samples were preserved, although with noticeable band shifts, particularly in 1712 and 1054 cm^{-1}. These shifts may be associated with the incorporation of nanoparticles. These findings are consistent with the XRD results. A similar result was observed in the study by De Oliveira Fontoura *et al.*,[3] where the same bands were identified in malt bagasse biochar produced by the hydrothermal method. The FTIR characterization therefore demonstrates that the P-doped hydrochar synthesized under milder conditions via the hydrothermal route is rich in different functional groups, acting as anchorage sites for metal precursor in the deposition of Co nanoparticles or bimetallic Co-Ni nanoparticles,[46] ensuring for such nanoparticle compositions outstanding catalytic activity in the generation of hydrogen from the hydrolysis of NaBH$_4$. The P content in the hydrochar was determined to be (0.200 ± 0.006)%, according to typical values for phosphorus-doped carbonaceous materials.[47,48] Furthermore, the presence of phosphorus as a dopant in the carbonaceous matrix confirms that it was not lost during material washing.

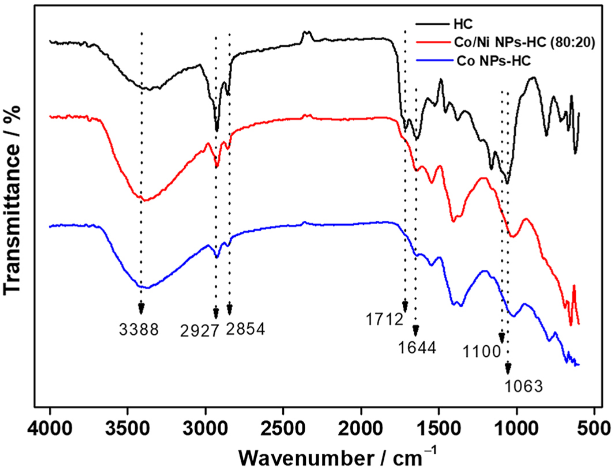

Figure 3. FTIR-ATR spectra obtained for the HC, Co NPs-HC, and Co/Ni NPs-HC (80:20).

The nitrogen physisorption isotherms are shown in Figure 4. The HC isotherm is classified as type IV, suggesting the presence of mesopores, while the Co NPs-HC and Co/Ni NPs-HC (80:20) materials exhibit type V isotherms, indicating the coexistence of micropores and mesopores.[49] The data related to the specific surface area, total pore volume, and average pore diameter of the materials are presented in Table 2. It is noted that HC has a lower specific surface area (0.07 m^2 g^{-1}) compared to Co/Ni NPs-HC (80:20) and Co NPs-HC, which presented surface areas of 14.10 and 26.24 m^2 g^{-1}, respectively. Furthermore, after Co and Ni NPs were incorporated into the hydrochar

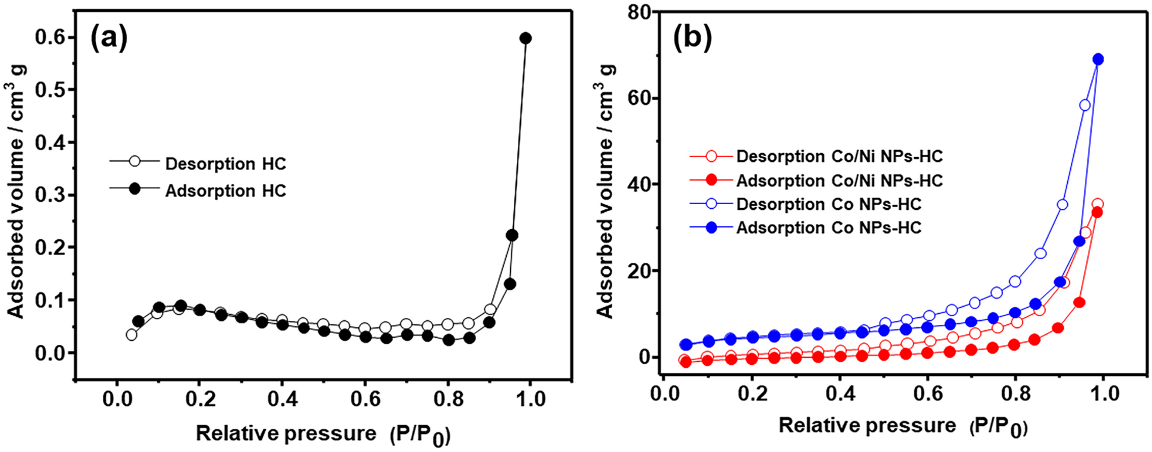

Figure 4. Nitrogen adsorption-desorption isotherm of (a) HC and (b) Co NPs-HC and Co/Ni NPs-HC (80:20).

Table 2. Textural properties of HC, Co NPs-HC, and Co/Ni NPs-HC (80:20) materials

Sample	Specific surface area / ($m^2 g^{-1}$)	Pore volume / ($cm^3 g^{-1}$)	Pore size / nm
HC[a]	0.07	0.001	16.62
Co NPs-HC[b]	26.23	0.112	1.93
Co/Ni NPs-HC (80:20)[c]	14.10	0.060	1.93

[a]HC: P-doped hydrochar; [b]Co NPs-HC: pure cobalt nanoparticles supported on P-doped hydrochar; [c]Co/Ni NPs-HC (80:20): bimetallic cobalt and nickel nanoparticles consisting of 80% Co and 20% Ni by mole supported on P-doped hydrochar.

surface, the average pore diameter was reduced from 16.62 to 1.93 nm.

Hydrogen evolution from $NaBH_4$

Initially, the composition of the nanoparticles supported on phosphorous-doped hydrochar was evaluated, and the results are presented in Figure 5. It is observed that HC presented the lowest efficiency in H_2 evolution (ca. 20%). Notably, Co NPs-HC demonstrated superior kinetics to nickel (Ni NPs-HC) and palladium (Pd NPs-HC) nanoparticles. However, the yields for Ni NPs-HC and Pd NPs-HC were slightly higher, at 63.5 and 56.4%, respectively, compared to Co NPs-HC, which showed a yield of 52.4%. The HGR for these materials were 1113.47 mL min^{-1} g^{-1} (Co NPs-HC), 712.52 mL min^{-1} g^{-1} (Ni NPs-HC), and 326.63 mL min^{-1} g^{-1} (Pd NPs-HC). Given the promising results obtained with HC supported with Co and Ni NPs, a bimetallic combination of these metals was also explored to investigate potential synergistic effects.

Different bimetallic Co and Ni NPs compositions were supported on HC and evaluated for H_2 evolution from $NaBH_4$. The results are presented in Figure 6a. It is noted that Co NPs-HC exhibited superior kinetics compared to the other NPs, as evidenced by the HGR values in Figure 6b. Additionally, the reaction yield decreased as the percentage of Ni increased, a phenomenon likely attributed to H_2 on the Ni surface, which hinders the adsorption of new BH_4^- anions and reduces catalytic efficiency.[50] Based on these findings, optimizing the H_2 evolution reaction using monometallic Co (Co NPs-HC) and bimetallic Co/Ni NPs-HC (80:20) nanoparticles as catalysts was decided.

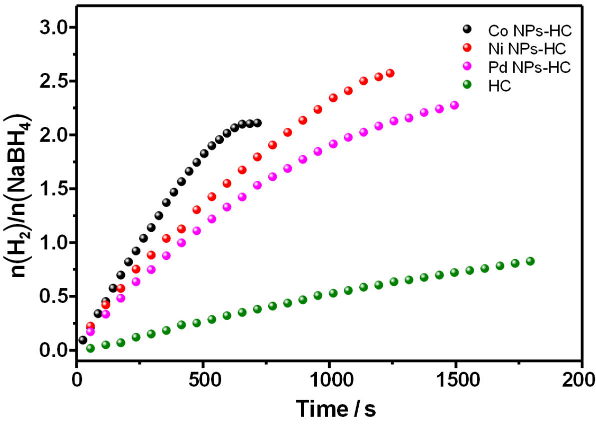

Figure 5. H_2 evolution from $NaBH_4$ to different metal nanoparticles (Co, Ni, or Pd) supported on hydrochar. Reaction conditions: 0.04 mmol of catalyst (8% relative to $NaBH_4$); 1.00 mL of $NaBH_4$ (0.500 mol L^{-1}); 10 mg of HC; temperature = 25 ºC.

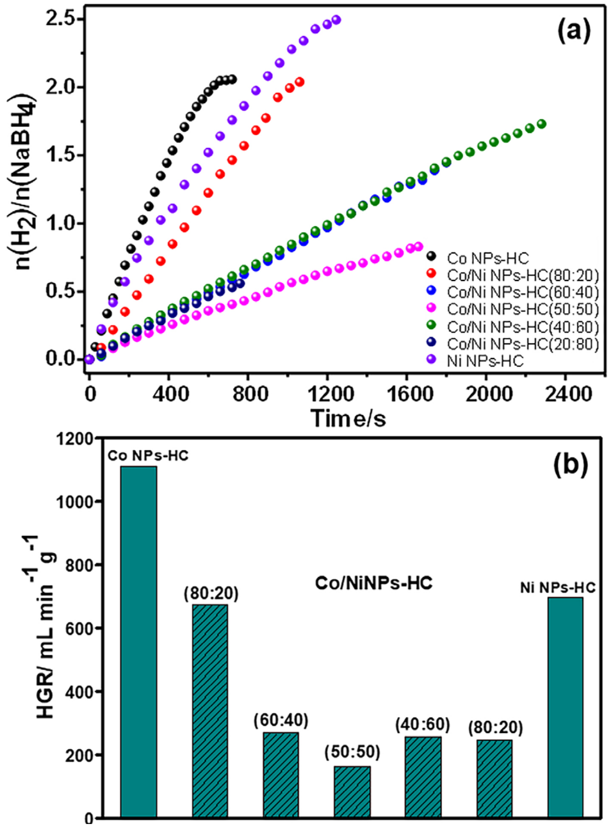

Figure 6. (a) H_2 evolution from $NaBH_4$ and (b) HGR for different compositions of Co and Ni nanoparticles supported on hydrochar. Reaction conditions: 0.04 mmol of catalyst (8% relative to $NaBH_4$); 1.00 mL of $NaBH_4$ (0.500 mol L^{-1}); 10 mg of HC; temperature = 25 ºC.

The addition of NaOH has been extensively studied, as $NaBH_4$ can be stabilized in an alkaline medium, and moderate NaOH concentrations can enhance the kinetics of hydrolysis.[51] However, at high concentrations, there may be a reduction in catalytic performance due to borate accumulation within the catalyst pores and the increased viscosity of the solution, which hinders the hydrolysis of

$NaBH_4$.[32,52] Consequently, the effect of varying NaOH concentrations was evaluated using Co NPs-HC and Co/Ni NPs-HC (80:20) as catalysts. The results are presented in Figure S2 (SI section). It was observed that increasing the NaOH concentration significantly improved the reaction kinetics for both Co NPs-HC and Co/Ni NPs-HC (80:20). Specifically, at a NaOH concentration of 0.5 mol L^{-1}, HGRs of 2193.17 and 1205.74 mL min^{-1} g^{-1} were achieved for Co NPs-HC and Co/Ni NPs-HC (80:20), respectively. Therefore, the use of 0.5 mol L^{-1} NaOH in the $NaBH_4$ hydrolysis reaction medium was considered in subsequent studies. Similar results obtained in the study conducted by Junior *et al.*[37] revealed that a catalyst made of Ni and Co nanoparticles supported on an electrolytic paste (Ni-Co NPs/EP) demonstrated enhanced catalytic activity for H_2 generation in a mildly alkaline medium, using a NaOH concentration of 0.05 mol L^{-1}.

Figure S3 (SI section) illustrates the effect of temperature on H_2 evolution during the hydrolysis of $NaBH_4$. The amount of H_2 generated increased proportionally with the rise in temperature. These results are consistent with previous studies[53,54] that also examined the influence of temperature on $NaBH_4$ hydrolysis, reporting an improvement in reaction kinetics as the temperature increases. Furthermore, the activation energy (E_a) was determined, revealing a value of 70.79 kJ mol^{-1} for Co/Ni NPs-HC (80:20) and 105.26 kJ mol^{-1} for Co NPs-HC. The low activation energy suggests the catalyst exhibits a diminished energy barrier, leading to accelerated reaction kinetics.[55]

Durability and reuse

The analysis of material reusability and longevity is crucial for potential industrial applications. Consequently, the durability and reusability of the nanocatalysts in H_2 evolution were assessed under the previously determined optimal conditions. Figure 7a illustrates the efficiency of the catalysts over five cycles, highlighting their durability. The monometallic nanocatalyst (Co NPs-HC) maintained its yield until the third cycle, while the bimetallic one (Co/Ni NPs-HC (80:20)) maintained its yield until the fourth, with a significant reduction in efficiency observed for both at the fifth cycle. This decline may be attributed to the blockage of active sites by sodium metaborate formed during the reaction, which decreases the availability of active sites for catalysis.[51] Figure 7b displays the results of catalyst reuse throughout the cycles. Both nanocatalysts maintained relatively constant efficiency up to the fourth cycle, with a noticeable decline in efficiency for the Co NPs-HC catalyst in the subsequent cycles. This decrease in efficiency may be attributed to catalyst leaching. On the other hand, Co/Ni NPs-HC (80:20) maintained the reaction yield until the sixth cycle, demonstrating better stability during its reuse. Thus, the nanocatalyst demonstrated stability and satisfactory performance throughout the evaluated cycles.[37] Additionally, the stability of the Co/Ni NPs-HC (80:20) catalyst was verified by TEM-EDS characterization after the reuse assay, with the results obtained being presented in Figure S4 (SI section). Thus, the morphological aspects verified for the fresh material were preserved after application in the hydrogen evolution reaction, i.e., the presence of graphene-like sheets referring to the HC decorated with Co-Ni bimetallic nanoparticles was observed, also proven by the EDS elemental analysis.

Catalytic reaction mechanism

The KIE is a valuable tool for probing the rate-determining step of a reaction. This effect can be classified

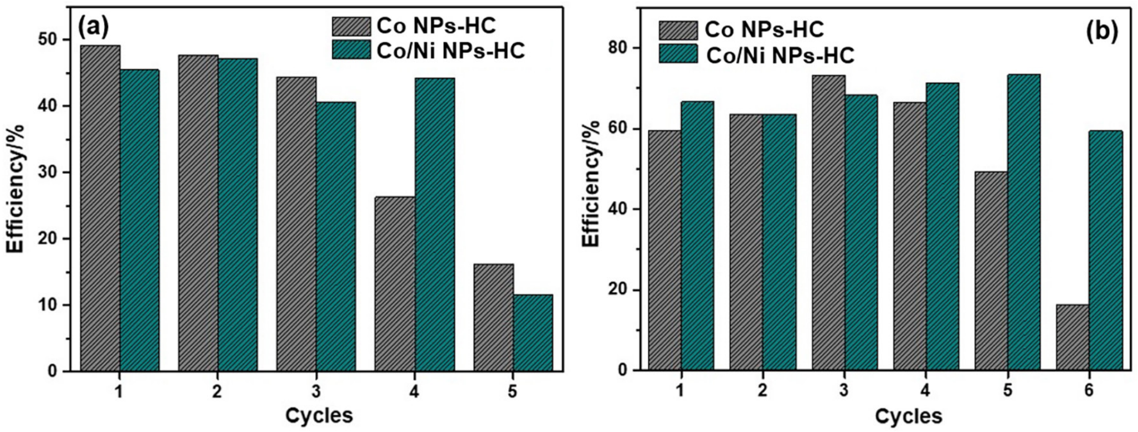

Figure 7. (a) Durability and (b) reusability of Co NPs-HC and Co/Ni NPs-HC (80:20) catalysts in H_2 evolution, evaluated in terms of efficiency. Reaction conditions: 0.04 mmol of catalyst (8% relative to $NaBH_4$); 1.00 mL of $NaBH_4$ (0.500 mol L^{-1}); 10 mg of HC; temperature = 25 °C.

as primary when KIE values range from 2 to 7, or secondary when they fall between 0.7 and 1.5. A primary KIE indicates that the formation or cleavage of a bond involving the isotopically substituted atom occurs during the rate-determining step. Conversely, a secondary KIE suggests that the rate-determining step does not directly involve such a bond, implying additional complexity.[56]

In this study, the KIE was evaluated for the Co/Ni NPs-HC catalyst during the hydrolysis of $NaBH_4$, and the results are presented in Figure 8. A KIE value of 3.96 was obtained, consistent with a primary isotopic effect. This result indicates that the reaction step involving water molecules constitutes the rate-determining step in the reaction.[57]

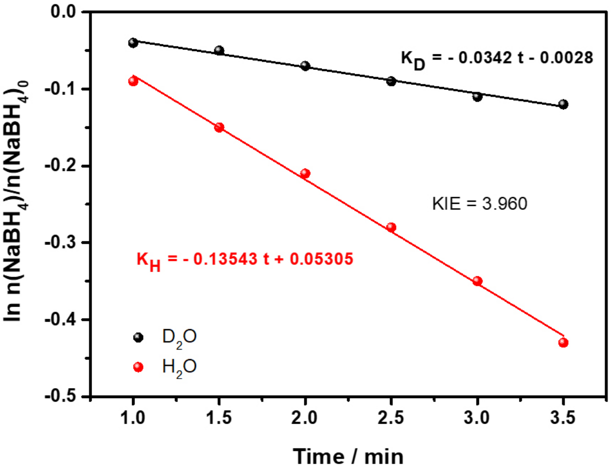

Figure 8. Kinetic isotope effect (KIE) on H_2 generation from $NaBH_4$ catalyzed by Co/Ni NPs-HC (80:20).

Comparison with literature

Table 3 provides examples of biochars derived from various materials used as supports for cobalt and nickel nanoparticles. The Co/Ni NPs-HC (80:20) catalyst exhibits a comparable or higher HGR regarding to the other reported catalysts and a greater number of reuse cycles. Consequently, Co/Ni NPs-HC (80:20) emerges as an excellent candidate for catalyzing the H_2 evolution reaction from $NaBH_4$.

Conclusions

In this study, it was developed and characterized a hydrochar derived from malt bagasse waste to support Co and Ni nanoparticles, which were utilized as nanocatalysts for hydrogen evolution from $NaBH_4$. The nanocatalysts were examined using various characterization techniques, including TEM, FTIR, XRD, and BET, to investigate their structure, morphology, and porosity. During the hydrogen evolution tests, the catalysts demonstrated notable catalytic efficiency, with hydrogen generation rates (HGR) of 2193.17 mL min^{-1} g^{-1} for Co NPs-HC and 1205.74 mL min^{-1} g^{-1} for Co/Ni NPs-HC (80:20). The activation energies were measured as 105.26 kJ mol^{-1} for Co NPs-HC and 70.79 kJ mol^{-1} for Co/Ni NPs-HC (80:20). Furthermore, the material exhibited stability, as evidenced by its reuse rate and durability over up to five cycles. These results underscore the significant potential of the developed catalyst for practical applications in hydrogen generation processes.

Supplementary Information

Supplementary information (EDS analysis and data of optimization of hydrogen evolution) is available free of charge at http://jbcs.sbq.org.br as PDF file.

Table 3. Evolution of H_2 from $NaBH_4$ using different catalysts

Catalyst	Reaction conditions	HGR / (mL min^{-1} g^{-1})	E_a / (kJ mol^{-1})	Reuse / cycles	Reference
Co@C	30 mg of catalyst, 1.5% in weight of $NaBH_4$, 1.5% in weight of NaOH, temperature = 30 ºC	1680	45.0	5	58
Co-PDA@BC	30 mg of catalyst, 1% in weight of $NaBH_4$, 1% in weight of NaOH, temperature = 25 ºC	25	31.3	5	59
BC/Co–B	100 mg of catalyst, 1.5% in weight of $NaBH_4$, 5% in weight of NaOH, temperature = 30 ºC	3887	56.4	5	60
Co/NiNPs-HC (80:20)	1.33 mg of catalyst, 1.89% in weight of $NaBH_4$, 2.0% in weight of NaOH, temperature = 25 °C	1205.74	70.79	6	this work

Co@C: carbon-confined cobalt; Co-PDA@BC: Cobalt supported on pistachio shell biochar modified with Polydopamine; BC/Co-B: bacterial cellulose biochar as a support for Com-B alloy. Co/Ni NPs-HC (80:20): bimetallic cobalt and nickel nanoparticles consisting of 80% Co and 20% Ni by mole supported on P-doped hydrochar. E_a: activation energy; HGR: hydrogen generation rate.

Data Availability Statement

All data supporting this article are available in the main text and supplementary information.

Acknowledgments

The authors are grateful to CAPES, CNPq (grant number: 405828/2022-5) and FAPEMIG (grant numbers: APQ-03113-22 and RED-00144-22) for the financial support.

Author Contributions

Marcela M. Ferreira was responsible for methodology, investigation, formal analysis, and writing original draft; Gessica C. Dias for methodology, investigation, formal analysis, and writing original draft; Tatianny A. Andradre for writing original draft, visualization, formal analysis, and writing review and editing; Iterlandes M. Junior for methodology, investigation, and formal analysis; José O. Marques Neto for the methodology, research, and formal analysis; Aline A. S. Silva for methodology, investigation, and formal analysis; Renata P. L. Moreira for conceptualization, supervision, resources, project administration, funding acquisition, and writing review and editing; Tiago A. Silva for conceptualization, supervision, resources, project administration, funding acquisition, and writing review and editing.

References

1. Lorente, A.; Remón, J.; Salgado, M.; Huertas-Alonso, A. J.; Sánchez-Verdú, P.; Moreno, A.; Clark, J. H.; *ACS Sustainable Chem. Eng.* **2020**, *8*, 18982. [Crossref]
2. García-Cubero, M. T.; Plaza, P. E.; Coca, M.; Lucas, S.; González-Benito, G.; *New Biotechnol.* **2016**, *33*, 88. [Crossref]
3. de Oliveira Fontoura, C. R.; Dutra, L. V.; Guezgüan, S. M.; Nascimento, M. A.; de Oliveira, A. F.; Lopes, R. P.; *J. Anal. Appl. Pyrolysis* **2022**, *168*, 105775. [Crossref]
4. Li, X.; Zhang, J.; Liu, B.; Su, Z.; *J. Cleaner Prod.* **2021**, *310*, 127428. [Crossref]
5. Beesley, L.; Moreno-Jiménez, E.; Gomez-Eyles, J. L.; Harris, E.; Robinson, B.; Sizmur, T.; *Environ. Pollut.* **2011**, *159*, 3269. [Crossref]
6. Tiihonen, A.; Siipola, V.; Lahtinen, K.; Pajari, H.; Widsten, P.; Tamminen, T.; Kallio, T.; Miettunen, K.; *Electrochim. Acta* **2021**, *368*, 137583. [Crossref]
7. González-Arias, J.; Sánchez, M. E.; Cara-Jiménez, J.; Baena-Moreno, F. M.; Zhang, Z.; *Environ. Chem. Lett.* **2022**, *20*, 211. [Crossref]
8. Baytar, O.; Şahin, Ö.; Ekinci, A.; *Fuel* **2023**, *346*, 128308. [Crossref]
9. Zhou, M.; Xu, Y.; Luo, G.; Zhang, Q.; Du, L.; Cui, X.; Li, Z.; *Chem. Eng. J.* **2022**, *432*, 134440. [Crossref]
10. Liu, B. H.; Li, Z. P.; *J. Power Sources* **2009**, *187*, 527. [Crossref]
11. Wang, Z.; Li, S.; Jin, Z.; Li, Z.; Liu, Q.; Zhang, K.; *Energy Strat. Rev.* **2023**, *45*, 101048. [Crossref]
12. Wang, W.; Herreros, J. M.; Tsolakis, A.; York, A. P. E.; *Energy* **2016**, *112*, 976. [Crossref]
13. Capurso, T.; Stefanizzi, M.; Torresi, M.; Camporeale, S. M.; *Energy Convers. Manage.* **2022**, *251*, 114898. [Crossref]
14. Schlapbach, L.; Züttel, A.; *Nature* **2001**, *414*, 353. [Crossref]
15. Bishnoi, A.; Pati, S.; Sharma, P.; *J. Power Sources* **2024**, *608*, 234609. [Crossref]
16. Huang, Z.; Cuevas, F.; Liu, X.; Jiang, L.; Wang, S.; Latroche, M.; Du, J.; *Int. J. Hydrogen Energy* **2009**, *34*, 9385. [Crossref]
17. Hai, T.; Alenizi, F. A.; Mohammed, A. H.; Chauhan, B. S.; Al-Qargholi, B.; Metwally, A. S. M.; Ullah, M.; *Int. Commun. Heat Mass Transfer* **2023**, *145*, 106848. [Crossref]
18. Madden, D. G.; O'Nolan, D.; Rampal, N.; Babu, R.; Çamur, C.; Al Shakhs, A. N.; Zhang, S.-Y.; Rance, G. A.; Perez, J.; Maria Casati, N. P.; Cuadrado-Collados, C.; O'Sullivan, D.; Rice, N. P.; Gennett, T.; Parilla, P.; Shulda, S.; Hurst, K. E.; Vitalie Stavila, V.; Allendor, M. D.; Silvestre-Albero, J.; Forse, A. C.; Champness, N. R.; Chapman, K. W.; Fairen-Jimenez, D.; *J. Am. Chem. Soc.* **2022**, *144*, 13729. [Crossref]
19. Gislon, P.; Prosini, P. P.; *Int. J. Hydrogen Energy* **2011**, *36*, 240. [Crossref]
20. United States Department of Energy (DOE); *Why Study Hydrogen Storage*, www.energy.gov/eere/fuelcells/hydrogen-storage, accessed in July 2025.
21. Uzundurukan, A.; Devrim, Y.; *Int. J. Hydrogen Energy* **2019**, *44*, 17586. [Crossref]
22. Al-shaikh, H.; Lasri, J.; Knight, J. G.; Al-Goul, S. T.; *Fuel* **2022**, *325*, 124962. [Crossref]
23. Liang, Y.; Dai, H.-B.; Ma, L.-P.; Wang, P.; Cheng, H.-M.; *Int. J. Hydrogen Energy* **2010**, *35*, 3023. [Crossref]
24. Şahin, Ö.; Saka, C.; Baytar, O.; Hansu, F.; *J. Power Sources* **2013**, *240*, 729. [Crossref]
25. Bennici, S.; Yu, H.; Obeid, E.; Auroux, A.; *Int. J. Hydrogen Energy* **2011**, *36*, 7431. [Crossref]
26. Ocon, J. D.; Tuan, T. N.; Yi, Y.; de Leon, R. L.; Lee, J. K.; Lee, J.; *J. Power Sources* **2013**, *243*, 444. [Crossref]
27. Kılınç, D.; Şahin, Ö.; *Int. J. Hydrogen Energy* **2019**, *44*, 18858. [Crossref]
28. Chou, C.-C.; Hsieh, C.-H.; Chen, B.-H.; *Energy* **2015**, *90*, 1973. [Crossref]
29. Paksoy, A.; Kurtoğlu, S. F.; Dizaji, A. K.; Altıntaş, Z.; Khoshsima, S.; Uzun, A.; Balcı, Ö.; *Int. J. Hydrogen Energy* **2021**, *46*, 7974. [Crossref]
30. Zhao, S.; Pan, Y.; *Sustainable Chem. Energy Mat.* **2025**, *1*, 100003. [Crossref]
31. Abraham, A.; Silviya, R.; Patel, R.; Patel, N.; Fernandes, R.; *Int. J. Hydrogen Energy* **2024**, *77*, 1245. [Crossref]

32. Souza, E. I. P.; Favero, U. G.; Sperandio, G. H.; Andrade, T. A.; Moreira, R. P. L.; Hespanhol, M. C.; *J. Environ. Chem. Eng.* **2025**, *13*, 116283. [Crossref]
33. Saka, C.; *Int. J. Hydrogen Energy* **2021**, *46*, 5150. [Crossref]
34. Severin, A. A.; Rauber, D.; Pachoula, S.; Philippi, F.; Radev, I.; Holtsch, A.; Müller, F.; Baumgärtner, M.; Hempelmann, R.; Kay, C. W. M.; *Sustainable Energy Fuels* **2023**, *7*, 752. [Crossref]
35. Gomes, P. B.; Bianchi, M. L.; Magalhães, F.; *Matéria* **2021**, *26*, e12965. [Crossref]
36. Pogorzelski, D. Q.; Santos, W. O.; Pimentel, G. G.; Ballotin, F. C.; Matias, P. C.; Vergütz, L.; *Rev. Bras. Ciênc. Solo* **2024**, *48*, e0230093. [Crossref]
37. Junior, I. M.; Sperandio, G. H.; Lopes, R. P.; *Int. J. Hydrogen Energy* **2024**, *53*, 1323. [Crossref]
38. Leichtweis, J.; Silvestri, S.; Welter, N.; Vieira, Y.; Zaragoza-Sánchez, P. I.; Chávez-Mejía, A. C.; Carissimi, E.; *Proc. Saf. Env. Prot.* **2021**, *150*, 497. [Crossref]
39. da Silva, A. D.; Silva, A. A. S.; da Silva, R. C.; Moreira, R. P. L.; Silva, T. A.; *Electroanalysis* **2024**, *36*, e202300425. [Crossref]
40. Zhu, K.; Liu, J.; Li, S.; Liu, L.; Yang, L.; Liu, S.; Wang, H.; Xie, T.; *Adv. Mater. Interfaces* **2017**, *4*, 1700377. [Crossref]
41. Gai, C.; Guo, Y.; Liu, T.; Peng, N.; Liu, Z.; *Int. J. Hydrogen Energy* **2016**, *41*, 3363. [Crossref]
42. Leichtweis, J.; Silvestri, S.; Stefanello, N.; Carissimi, E.; *Chemosphere* **2021**, *281*, 130987. [Crossref]
43. Fontana, K. B.; Chaves, E. S.; Sanchez, J. D. S.; Watanabe, E. R. L. R.; Pietrobelli, J. M. T. A.; Lenzi, G. G.; *Ecotoxicol. Environ. Saf.* **2016**, *124*, 329. [Crossref]
44. Franciskievicz, A. C.; Nicolin, D. J.; de Souza, F. B.; *Rev. Tecnol. Soc.* **2020**, *16*, 15. [Crossref]
45. Guo, Q.; Qiao, S.; Zhang, D.; Zhang, Z.; Yu, F.; Ma, Z.; Hu, Y.; *Biomass Bioenergy* **2024**, *182*, 107079. [Crossref]
46. Zhuang, X.; Liu, J.; Ma, L.; *Green Energy Environ.* **2023**, *8*, 1358. [Crossref]
47. Liu, C.; Shi, G.; Wang, G.; Mishra, P.; Jia, S.; Jiang, X.; Zhang, P.; Dong, Y.; Wang, Z.; *RSC Adv.* **2019**, *9*, 6898. [Crossref]
48. Zhao, L.; *RSC Adv.* **2017**, *7*, 13904. [Crossref]
49. Thommes, M.; Kaneko, K.; Neimark, A. V.; Olivier, J. P.; Rodriguez-Reinoso, F.; Rouquerol, J.; Sing, K. S. W.; *Pure Appl. Chem.* **2015**, *87*, 1051. [Crossref]
50. Netskina, O. V.; Tayban, E. S.; Rogov, V. A.; Ozerova, A. M.; Mukha, S. A.; Simagina, V. I.; Komova, O. V.; *Int. J. Hydrogen Energy* **2021**, *46*, 5459. [Crossref]
51. Sperandio, G.; Machado Jr., I. M.; Bernardo, E.; Moreira, R. P. L.; *Processes* **2023**, *11*, 3250. [Crossref]
52. Squizzatto, E. P.; Andrade, T. A.; Moreira, R. P. L.; Guimarães, L. M.; da Silva, M. J.; Novaes, F. J. M.; de Jesus, J. R.; *Processes* **2024**, *12*, 2677. [Crossref]
53. Li, Y.; Hou, X.; Wang, J.; Feng, X.; Cheng, L.; Zhang, H.; Han, S.; *Int. J. Hydrogen Energy* **2019**, *44*, 29075. [Crossref]
54. Didehban, A.; Zabihi, M.; Babajani, N.; *Polyhedron* **2020**, *180*, 114405. [Crossref]
55. Zhou, S.; Cheng, L.; Huang, Y.; Liu, Y.; Shi, L.; Isimjan, T. T.; Yang, X.; *Appl. Catal., B* **2023**, *328*, 122519. [Crossref]
56. Sperandio, G. H.; de Carvalho, J. P.; de Jesus, C. B. R.; Machado Jr., I. M.; de Oliveira, K. L. A.; Puiatti, G. A.; de Jesus, J. R.; Moreira, R. P. L.; *Int. J. Hydrogen Energy* **2024**, *83*, 774. [Crossref]
57. Bousada, G. M.; da Silva, V. N.; de Souza, B. F.;de Oliveira, R. S.; Machado Jr., I. M.; da Cunha, C. H. F.; Astruc, D.; Teixeira, R. R.; Moreira, R. P. L.; *RSC Adv.* **2024**, *14*, 19459. [Crossref]
58. Xu, D.; Zhang, X.; Zhao, X.; Dai, P.; Wang, C.; Gao, J.; Liu, X.; *Int. J. Hydrogen Energy* **2019**, *43*, 3702. [Crossref]
59. Akti, F.; *Int. J. Hydrogen Energy* **2022**, *47*, 35195. [Crossref]
60. Peng, C.; Li, T.; Zou, Y.; Xiang, C.; Xu, F.; Zhang, J.; Sun, L.; *Int. J. Hydrogen Energy* **2021**, *46*, 666. [Crossref]

Submitted: May 19, 2025
Final version online: August 13, 2025